European Journal of Medicinal Chemistry 247 (2023) 115046

Contents lists available at ScienceDirect

European Journal of Medicinal Chemistry

journal homepage: www.elsevier.com/locate/ejmech

Research paper

Synthesis, biological evaluation of novel iridium(III) complexes targeting mitochondria toward melanoma B16 cells

Yuhan Yuan [1], Yuanyuan Zhang [1], Jing Chen, Chunxia Huang, Haimei Liu, Wenlong Li, Lijuan Liang, Yi Wang, Yunjun Liu [*]

School of Pharmacy, Guangdong Pharmaceutical University, Guangzhou, 510006, PR China

ARTICLE INFO

Keywords:
Iridium(III) complexes
Apoptosis
Cell cycle arrest
RNA-sequence
Antitumor in vivo

ABSTRACT

A new ligand 2-(1*E*,3*E*,5*E*,7*E*)-2,6-dimethyl-8-(2,6,6-trimethylcyclohex-1-yl)octa-1,2,5,7-tetraen-1-yl)-1*H*-imidazo[4,5-f][1,10]phenanthroline (DTOIP) was synthesized and combined with $[Ir(ppy)_2Cl]_2{\cdot}2H_2O$ (ppy = deprotonated Hppy: 2-phenylpyridine), $[Ir(piq)_2Cl]_2{\cdot}2H_2O$ (piq = deprotonated Hpiq: 1-phenylisoquinoline) and $[Ir(bzq)_2Cl]_2{\cdot}2H_2O$ (bzq = deprotonated Hbzq: benzo[h]quinolone) to form $[Ir(ppy)_2(DTOIP)](PF_6)$ (**Ir1**), $[Ir(piq)_2(DTOIP)](PF_6)$ (**Ir2**), and $[Ir(bzq)_2(DTOIP)](PF_6)$ (**Ir3**), respectively. The complexes were characterized by elemental analysis, high-resolution mass spectrometry (HRMS), ^1H NMR and ^{13}C NMR. The antiproliferative activity of the complexes toward B16, BEL-7402, Eca-109 and normal LO2 cells was evaluated by 3-(4,5-dimethylthiazol-2-yl)-2,5-diphenyltetrazolium bromide (MTT) method. Complexes **Ir1**, **Ir2** and **Ir3** showed high antiproliferative activity against B16 cells with a low IC_{50} values of 0.4 ± 0.1, 2.0 ± 0.1 and 1.4 ± 0.09 μM, respectively. Three-dimensional (3D) in vitro cell models also demonstrated that the iridium(III) complexes have a remarkable cytotoxicity to B16 cells. The experiments of cellular uptake, mitochondrial localization, and intracellular distribution of the drugs proved that the three iridium(III) complexes can enter the mitochondria, leading to the loss of mitochondrial membrane potential (MMP), decreased glutathione (GSH) levels, causing an increase of intracellular ROS content, and DNA damage, finally inducing apoptosis. RNA-sequence and bioinformatics analyses were used to analyze the differentially expressed genes and enriched biology processes. Antitumor in vivo demonstrated that complex **Ir1** (5 mg/kg) exhibits a high efficacy to inhibit the tumor growth with an inhibitory rate of 71.67%. These results show that the complexes may be potent anticancer candidate drugs.

1. Introduction

Cancer is one of the most widespread serious diseases. It is characterized by uncontrolled growth of abnormal cells [1]. Due to the uncontrolled cell proliferation, invasion of surrounding and distant tissues aggressive metastasis, cancer is generally considered as a group of complex and multifaceted diseases [2] Chemotherapy is one of the common clinical treatments for cancer, which is usually combined with other methods such as radiotherapy and surgery to prolong cancer patient survival. Cisplatin, one of the representations of metal-based anticancer drugs, was the first transition metal drug that was used for chemotherapy. Its mechanisms were interfering with the aspect of DNA replication, repair, translation, or cell division [3]. Unfortunately, cisplatin kills both cancer and normal cells, which causes some serious side effects such as myelosuppression and hair loss, these side effects limited its clinical application [4]. This stimulated scientists to find anticancer compounds of other transition metals as alternative of cisplatin [5].

In recent years, nonplatinum anticancer drugs have received widespread attention, among these nonplatinum metal complexes, iridium-based metal compounds have been paid a great attention. Similar to platinum compounds, the properties of iridium(III) complexes such as redox potentials, ligand exchange kinetics and coordination numbers were widely studied. Not only in catalysts and optoelectronic sensors these transition metal complexes had a widespread application, but also in biological and medicinal fields, the anticancer activity of iridium(III) complexes has made a great achievement [6–25].

To obtain much information on the anticancer activity of iridium(III)

* Corresponding author.
E-mail address: lyjche@gdpu.edu.cn (Y. Liu).
[1] These authors contribute equally to this work.

https://doi.org/10.1016/j.ejmech.2022.115046
Received 7 October 2022; Received in revised form 12 December 2022; Accepted 21 December 2022
Available online 22 December 2022

complexes, in this paper, owing to (2*E*,4*E*,6*E*,8*E*)-3,7-dimethyl-9-(2,6,6-trimethylcyclohexen-1-yl)nona-2,4,6,8-tetraenal including multiple conjugate system, these conjugate system may produce a large influence on the biological activity, hence, we chose (2*E*,4*E*,6*E*,8*E*)-3,7-dimethyl-9-(2,6,6-trimethylcyclohexen-1-yl)nona-2,4,6,8-tetraenal as starting raw material to synthesize a novel polypyridyl ligand DTOIP (DTOIP = (2-(1*E*,3E,5*E*,7*E*)-2,6-dimethyl-8-(2,6,6-trimethylcyclohexen-1-en-1-yl) octa-1,3,5,7-tetraene-1-yl)-1*H*-imidazo[4,5-f][1,10]phenanthroline) and conjugated with three precursors, $[Ir(ppy)_2Cl]_2{\cdot}2H_2O$ (ppy = deprotonated Hppy: 2-phenylpyridine), $[Ir(piq)_2Cl]_2{\cdot}2H_2O$ (piq = deprotonated Hpiq: 1-phenylisoquinoline) and $[Ir(bzq)_2Cl]_2{\cdot}2H_2O$ (bzq = deprotonated Hbzq: benzo[h]quinolone) to synthesize three iridium (III) complexes: $[Ir(ppy)_2(DTOIP)](PF_6)$ (**Ir1**), $[Ir(piq)_2(DTOIP)](PF_6)$ (**Ir2**), $[Ir(bzq)_2(DTOIP)](PF_6)$ (**Ir3**) (Scheme 1). The complexes were characterized by elemental analysis, HRMS, ^{1}H NMR and ^{13}C NMR. The cytotoxicity of the complexes **Ir1**, **Ir2** and **Ir3** against cancer B16, BEL-7402, Eca-109 and normal LO2 cells was evaluated by 3-(4,5-dimethylthiazol-2-yl)-2,5-diphenyltetrazolium bromide (MTT) method. **Ir1**, **Ir2** and **Ir3** were found to be highly toxic to B16 in vitro. Since mitochondrial dysfunction is associated with pathological changes in many cancers, cardiovascular diseases and neurodegenerative disorders, studies on mitochondria as drug target point are of increasing interest. In this paper, we investigated the effects of the three complexes on targeting mitochondria, impact on mitochondrial and DNA damage, apoptosis mediated by intracellular ROS levels. We exploited RNA-sequence analysis to find the apoptotic pathways. Additionally, the antitumor activity in vivo was also explored.

2. Results and discussion

2.1. Synthesis and characterization

The ligand DTOIP was prepared through condensation of 1,10-phenanthroline-5,6-dione with (2*E*,4*E*,6*E*,8*E*)-3,7-dimethyl-9-(2,6,6-trimethylcyclohex-1-en-1-yl)nona-2,4,6,8-tetraenal in the presence of NH_4Ac and ethanol and refluxed for 6 h. After cooling to room temperature, the brown precipitate was obtained. The corresponding iridium(III) complexes were synthesized by direct reaction of DTOIP with the appropriate precursor complexes in a mixture of methanol/dichloromethane (Scheme 1) and purified by column chromatography. In the HRMS spectra, the determined molecular weights of the complexes are consistent with the expected values. In the ^{1}H NMR spectra, the five single peaks of chemical shifts less than 3 ppm are assigned to the five methyl groups, while chemical shift of 6.55 (s, 1H) in the ligand is attributed to the hydrogen at the position of C (h), the peak for the proton on nitrogen atom of the imidazole ring was not observed. This may be caused by metal coordination inducing electron deficiency in the ligand, therefore, the NH proton of the imidazole ring is very active and easy to be exchanged between the two imidazole nitrogen atoms in solution [26]. In the ^{13}C NMR spectra, the peaks of 64.8, 56.0, 56.9 and 55.9 ppm for DTOIP, **Ir1**, **Ir2** and **Ir3** are assigned to the C (u) atoms, the chemical shifts of 35.9, 34.7, 30.8 ppm for DTOIP, 33.9, 32.6, 18.5 ppm for **Ir1**, 33.9, 32.7, 18.8 ppm for **Ir2**, 33.9, 32.6, 18.7 ppm for **Ir3** are attributed to the carbon atoms of C (t), C (r) and C (v), respectively. The peaks of 23.6, 23.1, 20.8, 16.3, 14.6 ppm for DTOIP, 21.5, 18.5, 18.7, 14.4, 12.6 ppm for **Ir1**, 21,6, 19.1, 18.8, 14.4, 12.7 ppm for **Ir2**, 21.5, 19.0, 18.7, 14.3, 12.6 ppm for **Ir3** are attributed to the carbon atoms of five methyl groups. Hence, after the ligand DTOIP bonded with the metal to form complexes, a change of chemical shifts was observed.

The UV–Vis absorption spectra of 20.0 μM of **Ir1**, **Ir2**, **Ir3** in ethanol are presented in Fig. S1a (supporting information). Each complex exhibited two bands at wavelength of 257 (ε = 61,500) and 392 nm (ε = 48,000) for **Ir1**, 291 (ε = 68,500) and 385 nm (ε = 48,500) for **Ir2**, 253 (ε = 71,000) and 395 nm (ε = 49,500) for **Ir3**. The bands below 300 nm are assigned to the intraligand (IL) π–π* transitions, while the bands at 380–400 nm are attributed to the metal-to-ligand charge transfer transition. Fig. S1b (supporting information) shows the luminescence spectra of **Ir1** (0.4 μM), **Ir2** (2.0 μM), and **Ir3** (1.4 μM) in PBS buffer at room temperature, the maximum emission wavelengths appear at 599 nm for **Ir1**, 629 nm for **Ir2** and 609 nm for **Ir3**. The stability of the complexes in PBS solution was detected at 0 and 24 h, as shown in Fig. S1c (supporting information), no change of the peak shape was found, which suggests that the complexes are stable. The purity of the complexes was investigated by HPLC using methanol and water ($V_{methanol}$:V_{H2O} = 85:15 for **Ir1**, 90:10 for **Ir2** and 90:10 for **Ir3**) as mobile phase, during a period of 30 min, only a peak was observed, indicating that the complexes are pure (Fig. S1d) **(supporting information)**, the values of the purity for **Ir1**, **Ir2** and **Ir3** are 99.53, 96.85 and 98.28%, respectively.

2.2. pK_a determination

Charge is an important characteristic of drug molecules, since ionization sites determine the pK_a at a particular pH. The pK_a in turn can affect many parameters, including solubility, dissolution rate, reaction kinetics, formulation, cell permeability, tissue distribution, renal elimination, metabolism, protein binding and receptor interactions [27]. The pK_a value of the compound is a unique parameter specific to the chemical structure. According to Manallack, the pK_a distribution of drugs is mainly related to the nature of its functional groups, and the compounds with minimally one charge with a pK_a < 4 for acids and correspondingly a pK_a > 10 for bases can't cross the blood-brain barrier by passive diffusion [28]. The transport and distribution of most drugs are affected by passive diffusion, which depends on lipophilicity,

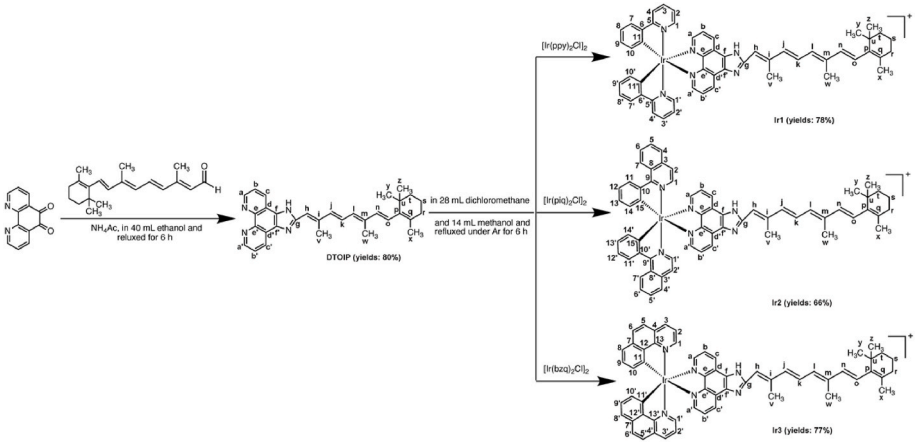

Scheme 1. Synthetic route for the ligand and complexes **Ir1**, **Ir2** and **Ir3**.

because of the need to cross the lipid barrier [29–31]. It is well known that the un-ionized form of drug is usually lipid soluble and diffuses readily across cell membranes. The pH range of the extracellular environment of tumor cells is about 6.7 [32]. The pH values of the complexes (100 μM) were determined to be 6.44 for **Ir1**, 6.52 for **Ir2** and 6.25 for **Ir3** dissolved in acetonitrile/water mixtures (v/v, 3:7). The pH was titrated by potentiometric titration with hydrochloric acid (100 mM) to reduce the pH to about 2.0. Then KOH solution (60 mM) was slowly titrated into the above solution and the change of pH was recorded. The pK_a value was obtained by plotting pH versus KOH volume. As shown in Fig. S2 (supporting information), the pK_a values are 6.12 for **Ir1**, 6.18 for **Ir2** and 6.32 for **Ir3**, respectively, indicating that **Ir1**, **Ir2**, **Ir3** have low ionization in the extracellular environment of tumor cells and can easily enter the tumor cells.

2.3. In vitro cytotoxicity determination

The in vitro cytotoxicity of **Ir1**-**Ir3** toward B16, BEL-7402, Eca-109 and normal LO2 cell was assessed by 3-(4,5-dimethylthiazol-2-yl)-2,5-diphenyltetrazolium bromide (MTT) method [33]. The obtained IC_{50} values are listed in Table 1, unexpectedly, the ligand DTOIP shows a certain degree cytotoxicity, but its cytotoxic activity is lower than those of iridium(III) complexes **Ir1**, **Ir2** and **Ir3**. Complexes **Ir1**, **Ir2**, **Ir3** exhibit high cytotoxic efficacy against the selected cancer cells. In particular, the complexes show very high cytotoxic activity toward B16 cells with a low IC_{50} value of 0.4 ± 0.1, 2.0 ± 0.1, 1.4 ± 0.09 μM for **Ir1**, **Ir2** and **Ir3**, respectively. Moreover, the cytotoxic activity of the complexes against B16, BEL-7402 and Eca-109 is higher than those of cisplatin and $[Ir(piq)_2(NPIP)](PF_6)$ (IC_{50} = 5.9 ± 0.5 μM, against B16) [9], but their cytotoxicity is lower toward BEL-7402 cells than our previous iridium(III) complex $[Ir(ppy)_2(dcdppz)](PF_6)$ (dcdppz = 11, 12-dichlorodipyrido[3,2-*a*:2′,3′-*c*]phenazine) [15]. According to Table 1, the anticancer activity of the complexes follows the order of **Ir1** > **Ir3** > **Ir2** toward B16, BEL-7402, Eca-109 and normal LO2 cells. Because the complexes show the highest cytotoxic efficacy against B16 cell among the selected cancer cells, this cell line was selected for the following cell experiments.

2.4. Cellular uptake and intracellular drug distribution

The pK_a values show that the complexes can enter the cell, the anticancer efficacy is closely related to the uptaken amount of the complexes by the cells. Therefore, the cell uptake of **Ir1**, **Ir2**, and **Ir3** by tumor cells was qualitatively and quantitatively studied under fluorescence microscopy and inductively coupled plasma mass spectrometry (ICP-MS), respectively. As shown in Fig. S3a (supporting information), after B16 cells were exposed to IC_{50} concentration of the complexes for 4 h, the cell nuclei were stained blue with 2-(4-amidinophenyl)-6-indolecarbamidine dihydrochloride (DAPI), the complexes emit green fluorescence, no complete overlap of the green and blue fluorescence was discovered, indicating that the complexes can enter the cells and mainly distribute in the cytoplasm.

In addition, to quantitatively explore the cellular uptake levels of **Ir1**, **Ir2** and **Ir3**, the accumulation of the three complexes in B16 cells was determined by ICP-MS. After a 4 h exposure of B16 cells to 20.0 μM complexes, the uptaken amounts are listed in Table 2, the uptaken amounts of **Ir1**, **Ir2** and **Ir3** are 168.00 ± 4.23, 51.67 ± 2.35 and 102.33 ± 3.55 ng metal/10^6 cells, which follows the order of **Ir1** > **Ir3** > **Ir2**, this is consistent with those of cytotoxic activity of the complexes against B16 cells. In general, the mitochondria and nuclei are important targets for drug, after the drugs enter the cells, the drugs may accumulate in the cytoplasm, mitochondria and nuclei, hence, the intracellular distribution among the cytoplasm, mitochondria and nuclei was determined used ICP-MS by isolating pure cellular compartments. After a treatment of B16 cells with 20.0 μM of the complexes for 4 h, the complexes enter the cell and most of the complexes accumulate in the cytoplasm and to a smaller extent in the mitochondria and nuclei (Table 2). Moreover, we found that the total amounts of the complexes **Ir1**, **Ir2** and **Ir3** distributing in the cytoplasm, mitochondria and nuclei are smaller than those of the cellular uptaken amounts. According to our previous work, we discovered that the iridium(III) complexes $[Ir(ppy)_2(PEYIP)](PF_6)$ (PEYIP = 2-phenethynyl-1*H*-imidazo[4,5-f][1,10]phenanthroline) [34] and $[Ir(piq)_2(IPPH)](PF_6)$ (IPPH = (2*S*,3*R*,5*S*,6*R*)-2-(2-(1*H*-imidazo[4,5-*f*][1,10]phenanthrolin-2-yl)phenoxy)-6-(hydroxymethyl)tetrahydro-2*H*-pyran-3,4,5-triol) [35] locate at the endoplasmic reticulum, while complexes $[Ir(ppy)_2(CPIP)](PF_6)$ (CPIP = 2-(4-chlorophenyl)-1*H*-imidazo[4,5-f][1,10]phenanthroline) [36] and $[Ir(ppy)_2(HMNPIP)](PF_6)$ (HMNPIP = 2-(1*H*-imidazo[4,5-f][1, 10]phenanthroline-3-yl)-6-methoxy-4-nitrophenol) [37] enter the lysosomes. Hence, besides entering the cytoplasm, mitochondria and nuclei, it is possible for the complexes to enter the lysosomes and endoplasmic reticulum, which results in a difference between the total cellular uptaken amounts and total amounts of the complexes distributing in the cytoplasm, mitochondria, and nuclei.

Table 1
IC_{50} values (μM) of iridium(III) complexes toward selected cancer cells for 48 h.

Complexes	B16	BEL-7402	Eca-109	LO2
DTOIP	2.6 ± 0.03	35.0 ± 4.1	19.1 ± 3.3	12.7 ± 0.3
Ir1	0.4 ± 0.1	5.2 ± 0.06	2.5 ± 0.07	7.1 ± 0.2
Ir2	2.0 ± 0.1	19.2 ± 0.4	4.8 ± 0.4	14.6 ± 0.7
Ir3	1.4 ± 0.09	6.1 ± 0.03	3.6 ± 0.05	7.5 ± 0.4
Cisplatin	19.8 ± 2.3	15.7 ± 3.1	11.6 ± 1.1	18.7 ± 2.5

Table 2
Uptaken amounts of the complexes in the cells and intracellular distribution (ng metal/10^6 cells).

complex	uptaken amount	cytoplasm	mitochondria	nuclei
Ir1	168.00 ± 4.23	38.00 ± 2.31	3.87 ± 0.64	2.01 ± 0.15
Ir2	51.67 ± 2.35	10.30 ± 1.02	2.11 ± 0.25	1.01 ± 0.04
Ir3	102.33 ± 3.55	29.83 ± 2.73	1.74 ± 0.11	1.33 ± 0.21

2.5. Inhibitory proliferation of iridium(III) complexes in 3D cells culture

The cells are usually cultured as monolayers on a flat surface, and these conditions do not accurately reflect what is happening in vivo because proper tissue structure and cell-cell contact are lost in this two-dimensional (2D) systems [38,39]. Three dimensional (3D) cells culture can better simulate the in vivo environment, which plays a very important role in the research of anti-cancer drugs [40,41]. Qualitative evaluation of the effect of **Ir1-3** on the growth of B16 cells was performed with live/dead staining (Calcein-AM/Hoechst 33342/PI). As shown in Fig. 1, B16 cells treated with IC_{50} concentration of **Ir1**, **Ir2** and **Ir3** for 24 h showed the number of live cells (green fluorescence) stained by Calcein-AM gradually decreased, and the number of dead cells stained with red fluorescence by PI gradually increased compared with those of untreated cells. The results indicate that the complexes can effectively inhibit the cell proliferation in B16 cells.

2.6. Cell cycle arrest determination

The cell cycle is closely related to the proliferation and development of tumor cells. Cell cycle arrest is commonly observed in many anti-tumor drugs [42,43]. Therefore, the drugs inhibit the proliferation of cancer cells through inhibiting the mitotic process of tumor cells. To evaluate the mechanism of the complexes inhibiting the cell growth, we used flow cytometry to the effects of the complexes on the cell cycle distribution. As shown in Fig. S4 (supporting information), the treatment of B16 cells (a) with IC_{50} concentration of **Ir1** (b), **Ir2** (c) and **Ir3** (d) for 24 h resulted in an increase of 41.65, 40.26 and 41.69% in the cell

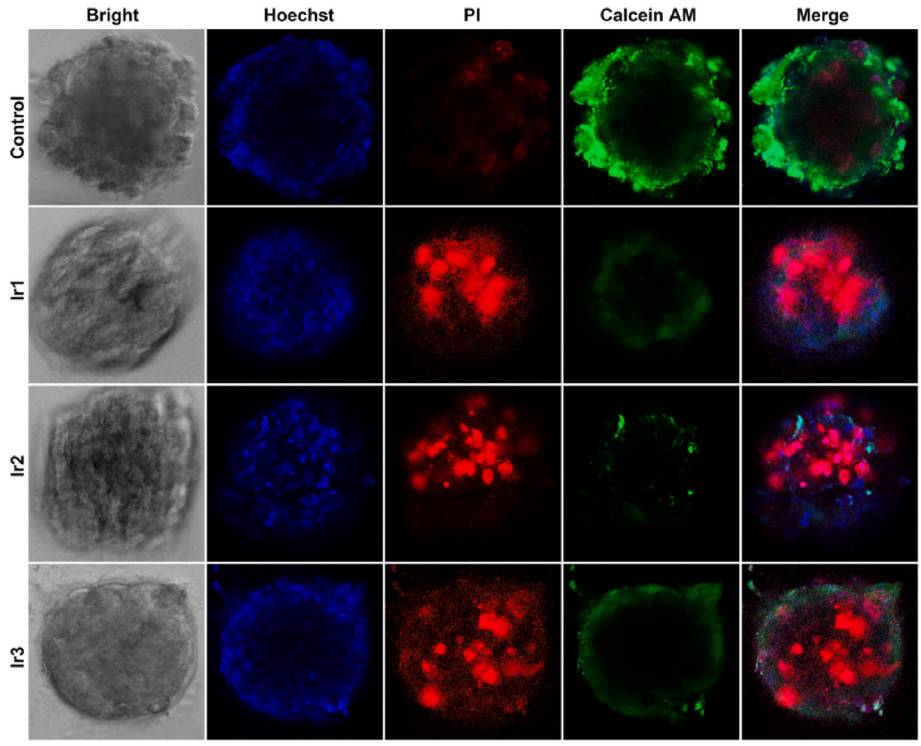

Fig. 1. 3D model of B16 cells stained with calcein AM and PI after a treatment with IC_{50} concentration of the complexes for 24 h.

at G0/G1 phase, accompanied by a corresponding reduction of percentage in the cell at S or G2/M phase. The results indicate that the complexes inhibit the cell growth at the G0/G1 phase. In our previous work, we found that the complexes $[Ir(piq)_2(NPIP)](PF_6)$ inhibit the cell growth at G2/M phase against B16 cells [9]. Therefore, we think that the different iridium(III) complexes inhibit the cell growth at the different phase toward the same cancer cells.

2.7. Mitochondrial depolarization

Mitochondria play a crucial role in apoptosis, necrosis, autophagy, and secretion of calcium ions [44]. The mitochondrial membrane potential (MMP, $\Delta\Psi_m$) is a fundamental characteristic reflecting the integrity of mitochondria [45]. The distribution of the complexes show that the complexes locate at the mitochondria, we also used microscope to observe the colocation of the complexes at the mitochondria. As shown in Fig. S5a (supporting information), the mitochondria were stained red with Mirotracker Red, while the complexes emit green fluorescence, the overlap of the red and green fluorescence indicates that the complexes locate at the mitochondria. The Pearson's colocalization coefficients (PCC) were calculated by analyzing the red and green fluorescence intensity (Image pro plus 6.0 software) in 50 cells according to literature [46]. The PCC values are 0.96 for **Ir1**, 0.97 for **Ir2** and 0.95 for **Ir3**, which indicated an existence of positive correlation.

The loss of MMP is characterized by an increase in green fluorescence (JC-1 monomer) and a decrease in red fluorescence (JC-1 aggregates) [47,48]. As shown in Fig. S5b (supporting information), incubation of B16 cells with IC_{50} concentration of **Ir1**, **Ir2** and **Ir3** causes a decrease in mitochondrial membrane potential, we observed that the red fluorescence intensity decreased, and the green fluorescence increased compared with the control. Owing to the complexes emitting weak green fluorescence, it is possible for the complexes to cause a cross-color interference with JC-1 monomer. To exclude the disturbance of the green fluorescence emitted by the complexes, we used flow cytometry to quantitatively determine the red fluorescence (JC-1 aggregates) and green fluorescence (JC-1 monomers), the complexes were used as reference. The green fluorescence intensity was calculated according to the following equation:

$$I_{\text{green fluorescence}} = I_{\text{complex in the cell+JC-1}} - I_{\text{complex in the cells}}$$

Where $I_{\text{complex in the cell+JC-1}}$ stands for the cells were treated with the complexes and then JC-1 was added, whereas $I_{\text{complex in the cells}}$ stands for the cells were treated with the complex (without JC-1).

As shown in Fig. S5c (supporting information), compared with the control, incubation of B16 cells with CCCP, IC_{50} concentration of **Ir1**, **Ir2**, **Ir3** led to a reduction of the ratio (R) of red/green fluorescence. These data also confirm that **Ir1**, **Ir2**, and **Ir3** can cause a decrease in MMP.

2.8. Intracellular reactive oxygen species (ROS) levels

2′,7′-dichlorofluorescindiacetate (DCFH-DA) can cross the cell membrane and is hydrolyzed by intracellular esterase to non-fluorescent 2′,7′-dichloro-3,6-fluorandiol (DCFH). In the presence of reactive oxygen species (ROS), DCFH is oxidized to the highly fluorescent dichlorofluorescein (DCF) [49]. Mitochondrial dysfunction are usually accompanied by the change of intracellular reactive oxygen species (ROS) levels, high levels of ROS can activate a variety of signal pathways which results in apoptosis and induce cell death [50,51]. To detect the change of intracellular ROS level, DCFH-DA was used as fluorescent probe. As shown in Fig. S6a (supporting information), the green fluorescence of B16 cells treated with IC_{50} concentration of **Ir1**, **Ir2**, and **Ir3** for 24 h increased significantly compared with that in the control, which indicates that **Ir1**, **Ir2**, and **Ir3** can induce the cells to produce more ROS and thus mediate apoptosis of B16 cells. To quantitatively compare the effect, the green fluorescence intensity was detected using flow cytometry (Fig. S6b, supporting information). Due to possible cross-color interference of weak green fluorescence emitted by the complexes with fluorescence probe, in the detection of intracellular ROS level, complexes were used as reference. The average green fluorescence intensity increased by 3.20, 3.95 and 5.30 times for **Ir1**, **Ir2** and **Ir3** compared with that in the control, respectively. These results further

show that **Ir1**, **Ir2** and **Ir3** can increase intracellular ROS levels.

2.9. Glutathione metabolism

Glutathione (GSH) is involved in scavenging reactive oxygen/nitrogen species (ROS/RNS) and is an antioxidant [52]. Glutathione metabolism intersects with most cell death pathways, such as apoptosis, autophagy, and necrosis [53]. High GSH levels shield cells from the activity of chemotherapeutic drugs [54]. Therefore, to potentiate the efficacy of drugs causing oxidative stress or avoiding acquired resistance to chemotherapy, we can further investigate the effect of the complexes on GSH metabolism. As shown in Fig. S7a (supporting information), we found that the GSH levels of cells treated by $2IC_{50}$ concentrations of **Ir1**, **Ir2**, and **Ir3** for 24 h were significantly lower than those of the control group. GSH reacts with lipid ROS and then forms glutathione disulfide (GSSG), a decrease of ratio of GSH/GSSG is considered to be a significant indicator of oxidative stress. Hence, we also determined the ratio of GSH/GSSG, as shown in Fig. S7b (supporting information), the ratio of GSH/GSSG reduced compared with that in the control after B16 cells were exposed to $2IC_{50}$ concentrations of **Ir1**, **Ir2**, and **Ir3** for 24 h, indicating an enhancement of oxidative stress. The results indicate that the complexes can induce a decrease of intracellular GSH levels and an increase of oxidative stress.

2.10. RNA-sequencing analysis

To explore the potential mechanism of action of **Ir1** on B16 cells, we used bioinformatics to investigate the key signaling pathways and biological processes in which the complex exerts its anti-tumor activity. We constructed volcano (Fig. 2a) and heat map (Fig. 2b) to show the distribution and expression of these genes. Fig. 2b shows that 306 genes were downregulated, and 337 genes were upregulated in B16 cells treated with $2IC_{50}$ concentration of **Ir1** for 24 h compared with the control group. Next, we performed Go analysis and found that system development, multicellular organism development and intracellular signal transduction were all biological processes that were significantly enriched in the **Ir1**-treated cells (Fig. 2c). KEGG pathway enrichment analysis revealed that **Ir1** affected several signaling pathways associated with cancer, including glutathione metabolism, PI3K/AKT and p53 signaling pathways (Fig. 2d).

2.11. Activation of endogenous apoptotic pathway

External aggression by a chemical compound sensed by the cells causes them to undergo two major forms of death, necrosis, and apoptosis [55]. Potential of **Ir1**-**Ir3** to induce B16 cell death was explored by AnnexinV/PI dual-labeling method. As shown in Fig. 3a, the percentage of early apoptotic cells (Q3) and late apoptotic cells (Q2) from 5.20% in the control (I) to 17.25% for **Ir1** (II), 15.97% for **Ir2** (III) and 16.07% for **Ir3** (IV), respectively. The increase in apoptotic population indicates the ability of complexes **Ir1**, **Ir2**, **Ir3** to induce apoptosis. The apoptotic ability follows the order of **Ir1** > **Ir3** > **Ir2**, which is line with those of cytotoxicity of the complexes toward B16 cells.

The RNA-sequencing analysis indicated that the complexes induce apoptosis via several signaling pathways. The apoptotic mechanism was researched by Western blot analysis. The Bcl-2 protein family determines the commitment of cells to apoptosis [56]. The enhanced expression of Bcl-2 makes it difficult for hematopoietic cells to die and promotes the accumulation of lymphocytes, which usually eventually leads to cancer death [57,58]. Caspase 3 is a major mediator of apoptosis activated during cellular exposure to cytotoxic drugs [59]. Many studies have shown that caspase 3 promotes stress-induced cancer cell growth,

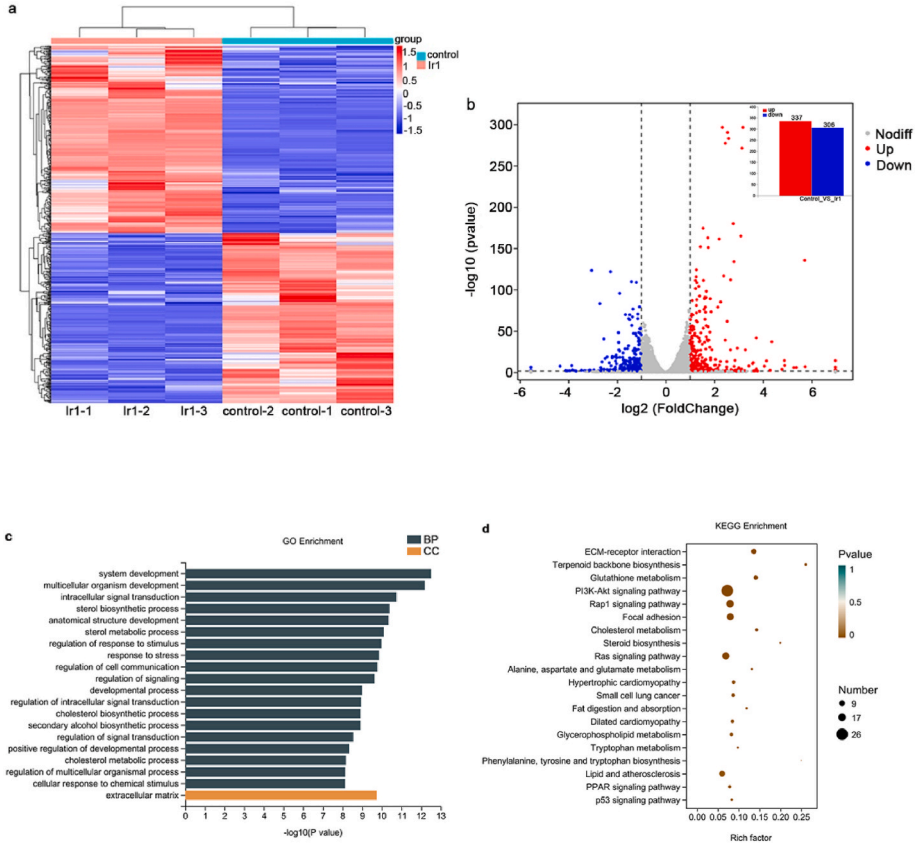

Fig. 2. Bioinformatics identified key pathways and biological processes associated with **Ir1** sensitivity in B16 cells. (a) Volcano map of **Ir1**. (b) Heat map of **Ir1** (inset: the number of up or downregulated genes). (c) GO analysis. (d) Kyoto Encyclopedia of Genes and Genomes pathway analyses.

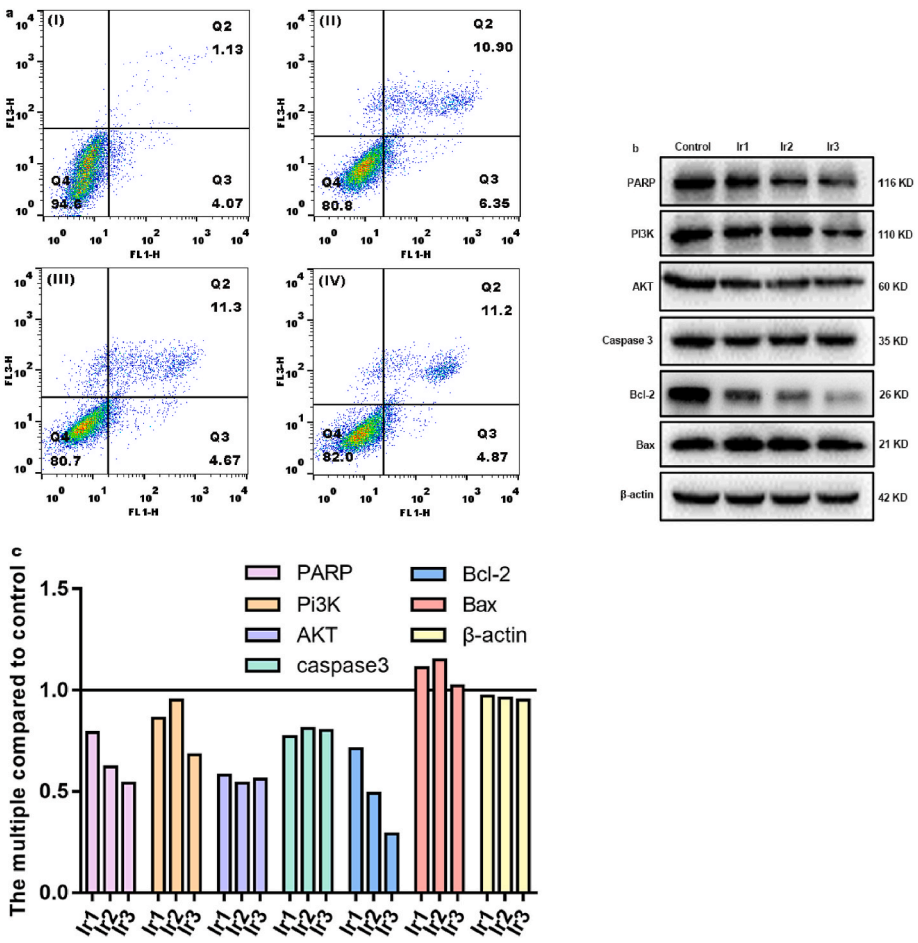

Fig. 3. (a) Apoptosis percentage of B16 (I) induced by IC_{50} concentration of **Ir1** (II), **Ir2** (III) and **Ir3** (IV) for 24 h, Q2, Q3, Q4 stand for late, early apoptosis and living cells. (b and c) Expression of cleaved PARP, PI3K, AKT, caspase 3, Bcl-2 and Bax in B16 cells exposure to IC_{50} concentration of **Ir1**, **Ir2** and **Ir3** for 24 h.

cellular migration, invasiveness, and tumor angiogenesis [60–62]. Poly ADP-ribose polymerase (PARP) is one of the most important substrates of caspase 3, which is associated with DNA repair and gene integrity [63]. Initiator caspases lead to the processing of executioner caspase 3, subsequently mediating the apoptotic cascade, including PARP cleavage [64]. Many studies have shown that PI3K (phosphatidylinositol 3-kinase)/AKT (protein kinase B) signaling pathway components are frequently altered in human cancers and that the PI3K/AKT pathway may play a decisive role in drug resistance phenotypes. In addition, AKT and PI3K have gene amplification in tumor cells [65], hence, we need to inhibit the expression of AKT and PI3K in tumor cells. As shown in Fig. 3b and c, Bax (Bcl2-associated X) expression increased, PARP cleavage occurred, and Bcl-2, caspase 3, PI3K and AKT expression decreased in B16 cells treated with IC_{50} concentration of **Ir1**, **Ir2** and **Ir3** for 24 h. Taken together, we deduced that **Ir1**, **Ir2**, and **Ir3** can regulate the expression of apoptosis-related proteins and finally induce cell death through the intrinsic apoptotic pathway.

2.12. DNA damage experiment

Ataxia-telangiectasia mutated proteins (ATM) plays a critical role in DNA damage signaling originating at DNA double-strand breaks (DSBs) [66]. ATM can phosphorylate various targets to promote the cellular response to damage. An important ATM target in chromatin is the histone protein H2AX. The phosphorylated form of H2AX, is known as γ-H2AX [67]. The increase of γ-H2AX is a marker of DNA cleavage. As shown in Fig. S8a (supporting information), we can clearly observe that more bright green fluorescence was found compared with that in the control after a 24 h exposure of B16 cells to IC_{50} concentration of **Ir1**, **Ir2** and **Ir3**. The enhancement of the green fluorescence shows an increase of γ-H2AX level. In addition, we further investigated the expression of γ-H2AX. See from Fig. S8b (supporting information), the complexes can up-regulate the expression of γ-H2AX. All these results indicate that **Ir1**, **Ir2** and **Ir3** can remarkably increase the γ-H2AX level, which further demonstrates that the complexes can cause DNA damage, finally lead to apoptosis.

2.13. Antitumor activity in vivo

B16 cells with high activity were inoculated subcutaneously in mice and then grew into spherical tumors. To evaluate the antitumor efficacy, mice were injected with saline and **Ir1**. In addition, the body weights of mice and the tumor size were also monitored every day. From Fig. 4a, **and 4d**, tumors in the **Ir1** (2 mg/kg), **Ir1** (3 mg/kg) and **Ir1** (5 mg/kg) treated groups were significantly diminished compared to those in the saline group. Fig. 4b shows the relative tumor volumes in the saline and **Ir1** (2 mg/kg) treated groups, the tumors of the saline group grew rapidly and the relative tumor volumes of the mice in the saline group were significantly larger than those in the **Ir1** (2 mg/kg) treated group on 8th day. Fig. 4c shows that no significant changes were found in the body weight of mice in the saline and **Ir1** (2 mg/kg) treatment groups during the treatment of 8 days. In addition, on the 9th day, in the **Ir1**-treated group, the drug of **Ir1** (2 mg/kg) was not injected into the mice, we continue to observe the change of tumor volume and the weight of the mice, as shown in Fig. 4b, the relative tumor volume of mice in the **Ir1** (2 mg/kg) treated group increased rapidly after drug

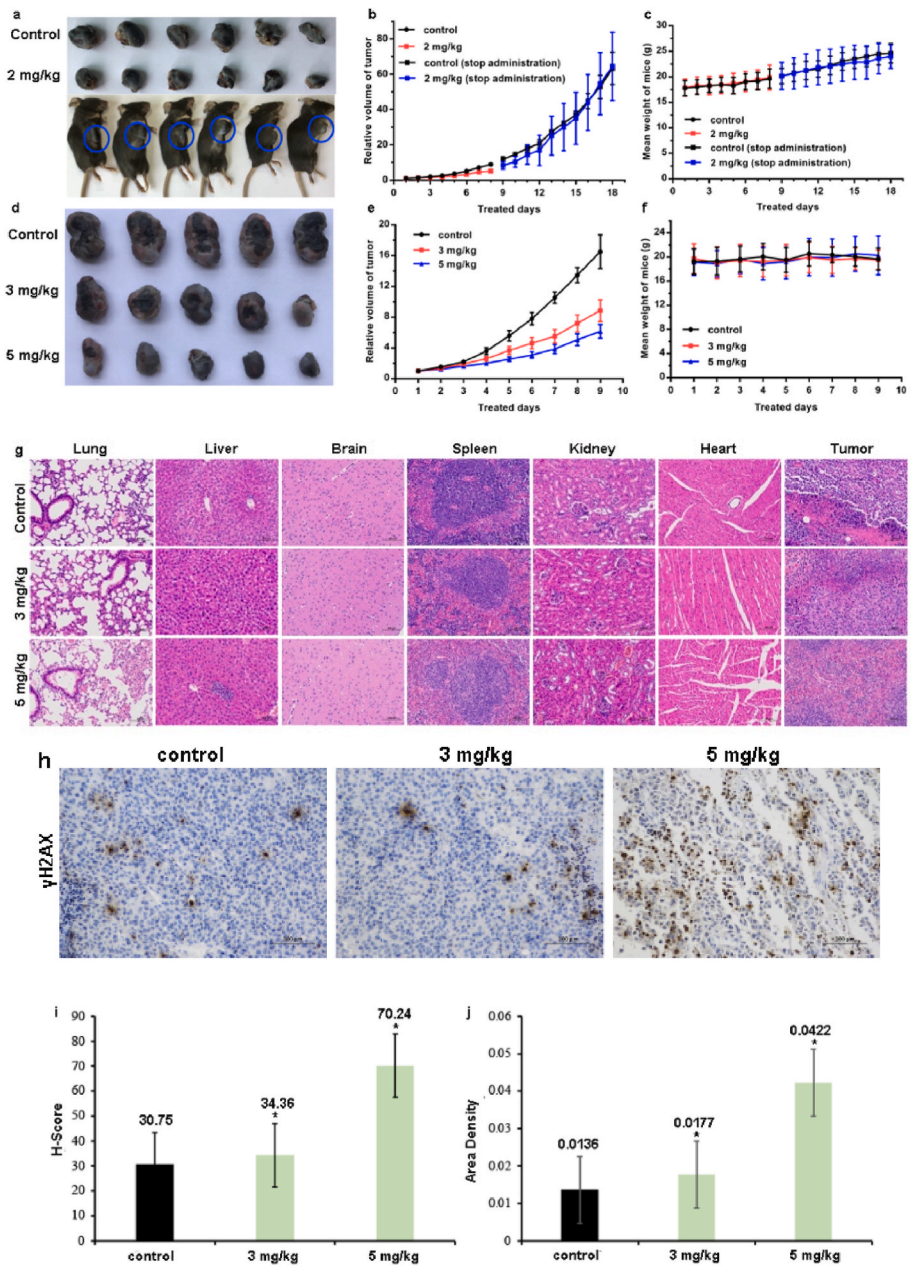

Fig. 4. The in vivo antitumor activity of **Ir1** (2 mg/kg), **Ir1** (3 mg/kg) and **Ir1** (5 mg/kg) toward B16 xenograft model. (a) Photographs of tumor in the vehicle group and **Ir1** (2 mg/kg) treatment group. (b) Relative tumor volumes and (c) mean weight of mice in the vehicle group and **Ir1** (2 mg/kg) treatment group. (d) Photographs of tumor in the vehicle group and **Ir1** (3 mg/kg, 5 mg/kg) treatment group. (e) Relative tumor volumes and (f) mean weight of mice in the vehicle group and **Ir1** (3 mg/kg, 5 mg/kg) treatment group. (g) H&E staining of lung, liver, brain, spleen, kidney, heart, and tumor. (h) γ-H2AX staining of tumor sections. (i and j) H-Score and Area density in the vehicle, 3 and 5 mg/kg of **Ir1**.

discontinuation, and it was approach to the relative tumor volume of mice in the saline group on the 18th day after drug discontinuation. From Fig. 4c, it was found that the body weight of mice in the saline group and **Ir1** (2 mg/kg) treated group showed an increasing trend after drug discontinuation. Fig. 4e shows the relative tumor volumes of mice in the saline, **Ir1** (3 mg/kg) and **Ir1** (5 mg/kg) treated groups. The tumors in the saline group grew rapidly, and the relative tumor volumes of mice in the saline group were significantly larger than those in the **Ir1** (3 mg/kg) and **Ir1** (5 mg/kg) drug-treated groups on the 9th day. Fig. 4f shows that no significant changes were found in the body weight of mice in the saline group, **Ir1** (3 mg/kg) and **Ir1** (5 mg/kg) drug-treated groups during the treatment. Taken together, the above experimental results showed that **Ir1** showed obvious inhibition of tumor growth, indicating that **Ir1** can exert a high inhibitory effect in vivo, while the effect of **Ir1** on the body weight of mice during treatment was close to that of the saline group, indicating that **Ir1** exerts anti-tumor efficacy with less effect on the body weight of mice. **Ir1** (2 mg/kg), **Ir1** (3 mg/kg) and **Ir1** (5 mg/kg) achieved an inhibitory rate of 42.57%, 56.14% and 71.67%, respectively, which also indicated that **Ir1** (5 mg/kg) showed a high antitumor efficacy.

To assess the toxic effects of **Ir1** in vivo, major organs (lung, liver, brain, spleen, kidney, heart) and tumors were stained by H&E staining in the saline, **Ir1** (3 mg/kg) and **Ir1** (5 mg/kg) drug-treated groups to determine the potential toxicity. As shown in Fig. 4g, compared with the saline-treated group, **Ir1**-treated groups exhibited no significant damage in the lung, liver, brain, kidney, and heart, only a massive proliferation of extramedullary hematopoietic cells within the red marrow was observed in the spleen. The above results suggest that **Ir1** has a good antitumor effect on B16 cells in vivo and is a powerful antitumor candidate for B16 cells. Since γ-H2AX is an important marker of DNA damage, γ-H2AX immunostaining can provide more insight into the anti-tumor mechanism. As shown in Fig. 4h, comparing with γ-H2AX in tumor sites of the saline group, **Ir1** (3 mg/kg) and **Ir1** (5 mg/kg) treated groups enhanced the expression of γ-H2AX, indicating that **Ir1** may cause DNA damage to exert antitumor effects. In addition, tumors from mice were stripped and analyzed for immunohistochemical positive area

intensity. We assessed the expression of γ-H2AX in tumors by calculating the Histochemistry score (H-score) and area density. As can be seen from Fig. 4i and j, both H-Score and area density are higher in the treated group than those in the control group, and the values in 5 mg/kg group are greater than those in the 3 mg/kg group. These data indicate that **Ir1** can significantly increase the expression level of γ-H2AX in mouse tumors.

3. Conclusions

In this study, we synthesized a new ligand DTOIP and three novel iridium(III) complexes, **Ir1**-**Ir3**, which are highly cytotoxic to B16 cells in vitro. The complexes can enter the cell in large quantities and can accumulate in the mitochondria. Meanwhile, the three complexes induce B16 cell cycle arrest in G0/G1 phase, which eventually triggers apoptosis. Mechanistic studies have shown that these complexes can induce apoptosis by depolarizing mitochondrial membranes, increasing intracellular ROS levels, decreasing intracellular GSH, causing DNA damage. In addition, RNA-sequencing analysis shows that the complexes cause apoptosis via several pathways including glutathione metabolism, PI3K/AKT and p53 signaling pathways. The Western blot analysis (PARP, PI3K, AKT, Caspase 3, Bcl-2 and Bax) confirmed that **Ir1**, **Ir2** and **Ir3** complexes induce apoptosis through inhibition of PI3K/AKT signaling pathway. The anti-tumor activity of **Ir1** in vivo demonstrated that **Ir1** has high anti-tumor activity with few toxic side effects and can improve the physical status of mice well. In summary, these results clearly indicate that these three complexes may induce apoptosis through the mitochondria-mediated pathway, inhibition of PI3K/AKT signaling pathway and the DNA damage pathway (Fig. 5). This work is helpful for the understanding the anticancer mechanism of iridium complexes.

4. Experimental

4.1. Materials and methods

Fetal Bovine Serum (FBS), newborn calf serum (NBCS), as well as the culture medium of RPMI (Roswell Park Memorial Institute) 1640 and DMEM (Dulbecco's Modified Eagle Medium) were all purchased from Gibco company. Ultrapure MilliQ water was used in all experiments. The cancer B16 (mouse melanoma cells), Eca-109 (human esophageal cancer cells), BEL-7402 (human hepatocellular carcinoma) and normal LO2 (human normal liver) cell lines were obtained from Sun Yat-Sen University (Guangzhou). Fluorescent probes and assay kits were purchased from Beyotime Biotechnology (Shanghai, China). $IrCl_3{\cdot}3H_2O$ was obtained from the Kunming Institution of Precious Metals. 2-phenylpyridine, benzo[h]quinoline, 1-phenylisoquinoline, 1,10-phenanthroline, (2*E*,4*E*,6*E*,8*E*)-3,7-dimethyl-9-(2,6,6-trimethylcyclohex-1-en-1-yl)nona-2,4,6,8-tetraenal, were purchased from Beijing HWRK Chemical Co., Ltd (Beijing). The HRMS spectra were measured by direct injection with Waters Xevo G2-XS QTof mass analyzer. ^{1}H NMR and ^{13}C NMR spectra were recorded on a Varian-500 spectrometer with dimethyl sulfoxide (DMSO-d_6) as solvent and tetramethylsilane (TMS) as an internal standard at 500 MHz at room temperature. UV–Visible and emission spectra were measured in the UV-2550 ultraviolet spectrophotometer and RF-5301PC fluorescence spectrophotometer (Shimadzu, Japan).

4.2. Synthesis of ligand and complexes

4.2.1. Preparation of ligand DTOIP

A mixture of 1,10-phenanthroline-5,6-dione (0.42 g, 2 mmol), (2*E*,4*E*,6*E*,8*E*)-3,7-dimethyl-9-(2,6,6-trimethylcyclohexen-1-yl)nona-2,4,6,8-tetraenal (0.57 g, 2 mmol) in ethanol (40 mL) and ammonium acetate (3.08 g, 40 mmol) was refluxed at 78 °C for 6 h. After cooling to room temperature, the yellow precipitate was washed three times with ice water, the yellow solid was obtained. Yield: 80%. Anal Calcd for $C_{32}H_{34}N_4$: C, 80.98, H, 7.22, N, 11.80%. Found: C, 80.82, H, 7.01, N, 11.98%. ^{1}H NMR (DMSO-d_6, 500 MHz): δ 9.01 (dd, 2H, $H_{a,a'}$, J = 1.5, J = 4.0 Hz), 8.54 (d, 2H, $H_{c,c'}$, J = 8.0 Hz), 7.82-7.79 (m, 2H, $H_{b,b'}$), 6.97-6.92 (m, 1H, H_j), 6.62 (d, 1H, H_o, J = 8.5 Hz), 6.55 (s, 1H, H_h), 6.33-6.25 (m, 1H, H_k), 6.22-6.17 (m, 2$H_{l,n}$), 2.69 (s, 3H, H_v), 2.20 (s, 3H, H_w), 2.02-1.95 (m, 2H, H_r), 1.90 (s, 3H, H_x), 1.70 (s, 3H, H_y), 1.58-1.55 (m, 2H, H_s), 1.46-1.43 (m, 2H, H_t), 1.02 (s, 3H, H_z). ^{13}C NMR (DMSO-d_6, 125 MHz): 152.3 ($C_{e,e'}$), 149.7 ($C_{a,a'}$), 145.6 (C_g), 143.9 (C_i), 139.4 (C_p), 139.2 (C_n), 138.9 (C_m), 133.9 (C_c), 133.3 ($C_{c'}$), 132.5 (C_j), 131.5 (C_d), 131.2 ($C_{d'}$), 129.7 (C_q), 128.8 (C_l), 127.0 (C_o), 125.3 (C_k), 121.9 ($C_{f,f'}$), 119.7 (C_b), 119.3 ($C_{b'}$), 117.3 (C_h), 64.8 (C_u), 35.9 (C_t), 34.7 (C_r), 30.9 (C_v), 23.6 (C_s), 23.1 (C_y), 20.8 (C_z), 16.3 (C_w), 14.6 (C_x). HRMS (CH_3CN) for $C_{32}H_{34}N_4$: m/z = 473.2803 ($[M-H]^-$).

4.2.2. Synthesis of complex [Ir(ppy)$_2$(DTOIP)] (PF_6) (*Ir1*)

Ir1 was prepared by refluxing *cis*-$[Ir(ppy)_2Cl]_2$ (0.292 g, 0.25 mmol)

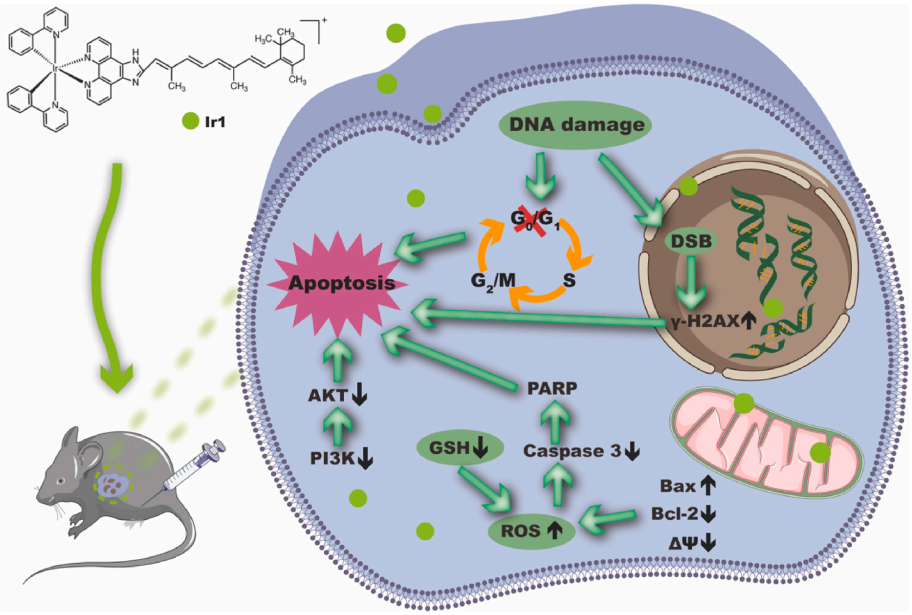

Fig. 5. Apoptotic mechanism of the complexes inducing B16 cells.

[68] and DTOIP (0.171 g, 0.5 mmol) in 45 mL of methanol/dichloromethane (V_{CH3OH}:V_{CH2Cl2} = 1:2, v/v) for 6 h under argon. At the end of the reaction, an excess of NH_4PF_6 was added and stirred for 2 h. The solution was filtered and concentrated to give a reddish brown solid. The crude product was then purified by neutral alumina column chromatography using dichloromethane and acetone as eluents. The yellow powder was obtained. Yield: 78%. Anal Cacld for $C_{54}H_{50}N_6PF_6Ir$: C, 57.90, H, 4.50, N, 7.50%. Found: C, 57.55, H, 4.91, N, 7.86%. ^{1}H NMR (DMSO-d_6, 500 MHz, Fig. S9a, supporting information): δ 9.04 (d, 2H, $H_{a,a'}$, J = 5.0 Hz), 8.25 (d, 2H, $H_{1,1'}$, J = 9.0 Hz), 8.11 (d, 2H, $H_{c,c'}$, J = 5.0 Hz), 8.04-8.01 (m, 2H, $H_{8,8'}$), 7.94 (d, 2H, $H_{7,7'}$, J = 8.0 Hz), 7.87 (t, 2H, $H_{8,8'}$, J = 7.5 Hz), 7.48 (d, 2H, $H_{10,10'}$, J = 5.5 Hz), 7.06 (t, 4H, $H_{9,9',4,4'}$, J = 7.5 Hz), 6.99-6.93 (m, 4H, $H_{3,3',2,2'}$), 6.67-6.43 (m, 2H, $H_{j,o}$), 6.34-6.18 (m, 4H, $H_{h,k,l,n}$), 2.67 (s, 3H, H_v), 2.24 (s, 3H, H_w), 2.07-2.01 (m, 2H, H_r), 1.90 (s, 3H, H_x), 1.70 (s, 3H, H_y), 1.60-1.56 (m, 2H, H_s), 1.48-1.43 (m, 2H, H_t), 1.02 (s, 3H, H_z). ^{13}C NMR (DMSO-d_6, 125 MHz, Fig. S9b, supporting information): 166.9 ($C_{e,e'}$), 152.4 (C_5), 152.1 ($C_{5'}$), 150.6 (C_a), 150.4 ($C_{a'}$), 149.1 ($C_{1,1'}$), 148.2 ($C_{6,6'}$), 145.4 (C_g), 143.9 (C_i), 139.2 (C_p), 138.7 (C_n), 137.6 (C_3), 137.3 ($C_{3'}$), 137.1 (C_m), 136.5 (C_c), 136.1 ($C_{c'}$), 135.4 (C_j), 132.2 (C_q), 132.1 (C_l), 131.7 (C_8), 131.2 ($C_{8'}$), 130.2 ($C_{10,10'}$), 129.9 (C_o), 129.6 (C_7), 129.3 ($C_{7'}$), 128.7 (C_k), 127.2 ($C_{9,9'}$), 126.9 ($C_{11,11'}$), 125.0 ($C_{d,d'}$), 123.8 ($C_{4,4'}$), 123.5 ($C_{f,f'}$), 122.3 ($C_{b,b'}$), 119.9 (C_h), 116.7 ($C_{2,2'}$), 56.0 (C_u), 33.9 (C_t), 32.6 (C_r), 28.8 (C_v), 21.5 (C_s), 18.7 (C_y), 18.5 (C_z), 14.4 (C_w), 12.6 (C_x). HRMS (CH_3CN, Fig. S9c, supporting information) for $C_{54}H_{50}N_6PF_6Ir$: m/z = 975.3721 ($[M - PF_6]^+$).

4.2.3. Synthesis of complex [Ir(piq)$_2$(DTOIP)] (PF_6) (**Ir2**)

The complex [Ir(piq)$_2$(DTOIP)](PF_6) was prepared in an identical manner described as **Ir1**, and *cis*-[Ir(ppy)$_2$Cl]$_2$ was replaced by *cis*-[Ir(piq)$_2$Cl]$_2$ [68]. Yield: 66%. Anal Calcd for $C_{62}H_{54}N_6PF_6Ir$: C, 61.02, H, 4.46, N, 6.87%. Found: C, 61.38, H, 4.84, N, 6.43%. ^{1}H NMR (DMSO-d_6, 500 MHz, Fig. S10a, supporting information): δ 9.02 (d, 4H, $H_{a,a',1,1'}$, J = 7.5 Hz), 8.41 (d, 2H, $H_{c,c'}$, J = 8.0 Hz), 8.03-7.89 (m, 6H, $H_{b,b',11,11',4,4'}$), 7.88-7.85 (m, 6H, $H_{2,2',5,5',6,6'}$), 7.43 (d, 2H, $H_{7,7'}$, J = 6.5 Hz), 7.37 (d, 2H, $H_{14,14'}$, J = 6.5 Hz), 7.18 (t, 2H, $H_{12,12'}$, J = 7.0 Hz), 6.96 (t, 2H, $H_{13,13'}$, J = 7.5 Hz), 6.67-6.44 (m, 2H, $H_{j,o}$), 6.34-6.18 (m, 4H, $H_{h,k,l,n}$), 2.67 (s, 3H, H_v), 2.23 (s, 3H, H_w), 2.05-1.98 (m, 2H, H_r), 1.91 (s, 3H, H_x), 1.70 (s, 3H, H_y), 1.60-1.51 (m, 2H, H_s), 1.48-1.42 (m, 2H, H_t), 1.02 (s, 3H, H_z). ^{13}C NMR (DMSO-d_6, 125 MHz, Fig. S10b, supporting information): 167.9 ($C_{9,9'}$), 152.8 (C_e), 152.5 ($C_{e'}$), 151.9 ($C_{a,a'}$), 148.3 ($C_{10,10'}$), 148.3 ($C_{1,1'}$), 148.2 (C_g), 145.4 (C_i), 143.9 (C_p), 142.1 (C_n), 140.8 (C_m), 137.7 (C_3), 137.5 ($C_{3'}$), 137.4 (C_j), 137.3 (C_5), 137.2 ($C_{5'}$), 136.6 (C_q), 132.1 (C_l), 131.7 ($C_{12,12'}$), 130.7 (C_{14}), 130.6 ($C_{14'}$), 129.4 ($C_{c,c'}$), 128.8 (C_o), 128.4 ($C_{7,7'}$), 127.7 (C_{11}), 127.3 ($C_{11'}$), 127.0 (C_k), 126.5 ($C_{13,13'}$), 125.6 ($C_{6,6'}$), 124.7 ($C_{15,15'}$), 123.6 ($C_{4,4'}$), 122.4 ($C_{8,8'}$), 122.2 ($C_{d,d'}$), 116.7 ($C_{f,f'}$), 114.7 ($C_{b,b',h}$), 111.8 ($C_{2,2'}$), 56.9 (C_u), 33.9 (C_t), 32.7 (C_r), 28.9 (C_v), 21,6 (C_s), 19.1 (C_y), 18.8 (C_z), 14.4 (C_w), 12.7 (C_x). HRMS (CH_3CN, Fig. S10c, supporting information) for $C_{62}H_{54}N_6PF_6Ir$: m/z = 1075.4601 ($[M - PF_6]^+$).

4.2.4. Synthesis of complex [Ir(bzq)$_2$(DTOIP)](PF_6) (**Ir3**)

Ir3 was synthesized in an identical manner described as **Ir1** and *cis*-[Ir(ppy)$_2$Cl]$_2$ was replaced with *cis*-[Ir(bzq)$_2$Cl]$_2$.[68] Yield: 77%. Anal Calcd for $C_{58}H_{50}N_6PF_6Ir$: C, 59.63, H, 4.31, N, 7.19%. Found: C, 59.24, H, 4.74, N, 7.55%. ^{1}H NMR (DMSO-d_6, 500 MHz, Fig. S11a, supporting information): δ 9.05 (d, 2H, $H_{a,a'}$, J = 8.0 Hz), 8.51 (d, 2H, $H_{1,1'}$, J = 8.0 Hz), 8.10 (d, 2H, $H_{c,c'}$, J = 4.5 Hz), 7.99-7.93 (m, 4H, $H_{3,3',8,8'}$), 7.92-7.87 (m, 4H, $H_{5,5',6,6'}$), 7.57 (d, 2H, $H_{10,10'}$, J = 8.0 Hz), 7.45-7.43 (m, 2H, $H_{9,9'}$), 7.22 (t, 2H, $H_{b,b'}$, J = 7.0 Hz), 7.07-6.96 (m, 2H, $H_{2,2'}$) 6.64-6.45 (m, 2H, $H_{j,o}$), 6.32-6.17 (m, 4H, $H_{h,k,l,n}$), 2.67 (s, 3H, H_v), 2.22 (s, 3H, H_w), 2.04-1.98 (m, 2H, H_r), 1.91 (s, 3H, H_x), 1.70 (s, 3H, H_y), 1.60-1.55 (m, 2H, H_s), 1.48-1.43 (m, 2H, H_t), 1.03 (s, 3H, H_z). ^{13}C NMR (DMSO-d_6, 125 MHz, Fig. S11b, supporting information): 156.4 ($C_{e,e'}$), 152.4 ($C_{a,a'}$), 148.8 (C_1), 148.7 ($C_{1'}$), 147.2 ($C_{13,13'}$), 144.4 (C_g), 143.6 (C_i), 141.8 (C_p), 140.3 (C_n), 138.3 (C_m), 137.5 (C_3), 137.3 ($C_{3'}$), 137.1 ($C_{7,7'}$), 136.5 ($C_{c,c'}$), 133.7 (C_j), 132.2 (C_q), 130.5 (C_l), 130.5 ($C_{12,12'}$), 129.7 (C_o), 129.5 ($C_{4,4'}$)), 129.3 ($C_{5,5'}$), 128.5 ($C_{8,8'}$), 127.2 ($C_{6,6'}$), 126.9 ($C_{11,11'}$), 126.7 ($C_{k,d,d'}$), 126.4 ($C_{9,9'}$), 124.2 ($C_{10,10'}$), 122.7 ($C_{2,2',f,f'}$), 120.3 ($C_{b,b'}$), 116.8 (C_h), 55.9 (C_u), 33.9 (C_t), 32.6 (C_r), 28.8 (C_v), 21.5 (C_s), 19.0 (C_y), 18.7 (C_z), 14.3 (C_w), 12.6 (C_x). HRMS (CH_3CN, Fig. S11c, supporting information) for $C_{58}H_{50}N_6PF_6Ir$: m/z = 1023.3757 ($[M - PF_6]^+$).

4.3. Purity determination of the complexes

The purity of the complexes was analyzed by COSMOSIL 5C_{18}-MS-II column (250 mm × 10 mm) on 25 °C. We used H_2O with 0.1% trifluoroacetic acid (TFA) as mobile phase A and methanol with 0.1% TFA as mobile phase B with a flow rate of 3 mL/min. The different elution programs eluted the complexes **Ir1**, **Ir2** and **Ir3**. The elution program of **Ir1** was H_2O (0.1% TFA): MeOH (0.1% TFA) = 15:85, **Ir2** was 10:90 and **Ir3** was 10:90, and the detection wavelength was set at 257 nm, 291 nm and 253 nm.

4.4. pK_a determination

The pKa values of the complexes were determined by potentiometric titration using a pH meter (Basic pH Meter PB-10, Sartorius), calibrated with standard buffers of pH 4.01, 6.86 and 9.18. The complexes **Ir1**, **Ir2** and **Ir3** (1.0 mM) were dissolved in acetonitrile and water (v/v, 3:7), and adjusted pH values to 2 with hydrochloric acid (100 mM). Then, titration was then performed with KOH (60 mM).

4.5. Cell culture

B16, Eca-109, LO2 were cultured in Dulbecco's Modified Eagle Medium (DMEM) containing 10% heat-inactivated fetal bovine serum (FBS) and penicillin (100 U/ml)/streptomycin (0.1 mg/ml) (both Gibco). BEL-7402 were cultured in Roswell Park Memorial Institute 1640 (RPMI 1640) supplemented with 10% FBS, penicillin (100 U/mL)/streptomycin (0.1 mg/mL).

4.6. Cytotoxicity assay in vitro

Cytotoxicity of **Ir1**-**Ir3** were evaluated against the cancer and normal cell lines using the MTT assay. The various cell lines were seeded in 96-well plate at a density of 2000 cells/well overnight. Then, seven different concentrations (100, 50, 25, 12.5, 6.25, 3.125, 1.56 μM) of **Ir1**, **Ir2**, **Ir3** and DTOIP (complexes and ligand were dissolved in DMSO, the final concentration of DMSO is 0.05%) were added to the wells individually, after 48 h of incubation, MTT (9:1, v/v) was added into every well and incubated at 37 °C for 4 h. The purple formazan product was dissolved with 100 μL dimethyl sulfoxide. Finally, the cell viability was measured at a wavelength of 490 nm using a microplate reader. The mean values were obtained through three independent experiments.

4.7. Cellular uptake

B16 cells were inoculated in 12-well plates at a density of 4 × 10^4 cells/well. The cells were treated with IC_{50} concentration of **Ir1**, **Ir2** and **Ir3** for 4 h. Then the cells were stained with DAPI (1:100) incubated at 37 °C for 20 min in dark and observed under ImageXpress R Micro XLS System (MD company, USA).

The cell uptake was quantitatively determined by inductively coupled plasma-mass spectrometry (ICP-MS, Thermo Fisher Scientific iCAP Qc). B16 cells (5 × 10^5 cells/well) were seeded in 6-well plate and incubated with 20.0 μM of **Ir1**, **Ir2** and **Ir3** for 4 h when the cells arrived logarithmic phase. Then, washing the adherent cells twice with PBS containing 5 mM EDTA. After trypsinization and centrifugation of the suspension at 800 rpm for 5 min, repeating the above processes till the residual complexes were completely removed. The cells were digested

with 60% HNO_3 at 60 °C to completely release the uptaken iridium(III) complexes from the cells and then a 5 mL solution was obtained by adding Milli-Q water. The uptaken mounts were calculated through the following procedures: (I) determining the intensity (^{193}Ir) of different concentrations of iridium standard solution, through linear fitting to obtain a fitting equation (x-axis: concentration of sample; y-axis: intensity). (II) determining the intensity (^{193}Ir) in the sample, then calculate the uptaken amount according to the fitting equation.

4.8. Intracellular drug distribution

Intracellular distribution of the complexes was tested using inductively coupled plasma mass spectrometry (ICP-MS). B16 cells treated with 20.0 μM **Ir1**, **Ir2** and **Ir3** for 4 h were collected separately and washed four times with PBS containing EDTA. The number of cells were same in each sample when detecting the distribution of the complexes in the mitochondria, cytoplasm, nucleus. Then cytoplasm, nucleus and mitochondria were extracted according to the corresponding organelle extraction kit (BestBio, Shanghai). All the samples were digested with nitric acid overnight and detected by ICP-MS.

4.9. Cytotoxicity of iridium(III) complexes in 3D cells culture

Add 150 μL of Matrigel matrix (8 mg/mL) to the bottom of the confocal dish, and then incubated at 37 °C for 30 min. A549 cells in the exponential growth phase were trypsinized to obtain a single-cell suspension. Approximately 4×10^4 diluted A549 cells were transferred to Matrigel-coated confocal dishes. Then 200 μL of the substrate mixture (0.8 mg/mL) was gently added to the confocal culture dish to form a gel-cell-gel structure and incubated continuously for 6 days. To determine the cytotoxicity of iridium(III) complexes, the cells of 3D multicellular tumor spheroids cultured with IC_{50} concentration of **Ir1**, **Ir2** and **Ir3** for 24 h were stained with Calcein-AM/Hoechst 33342/PI and observed under a confocal microscopy (Leica, TCS SP8 SR).

4.10. RNA sequencing analysis

B16 cells were inoculated in 6-well culture plates (5×10^5 cells) and incubated in a 37 °C incubator for 24 h. The growing B16 cells were exposed to **Ir1** at a concentration of $2IC_{50}$ for 24 h. Adherent cells were washed twice using pre-chilled PBS. The appropriate amount of RNA extraction solution (Servicebio, China) was added, and cells were well blown using a pipette to lyse them adequately, followed by isolation of total RNA using Trizol Reagent (Invitrogen Life Technologies), after which the concentration, quality and integrity were determined using a NanoDrop spectrophotometer (Thermo Scientific). Sequencing libraries were generated using the TruSeq RNA Sample Preparation Kit (Illumina, San Diego, CA, USA). To select cDNA fragments with a length of preferably 200 bp, library fragments were purified using the AMpure XP system (Beckman Coulter, Beverly, CA, USA). The library fragments were then quantified using Agilent high-sensitivity DNA analysis on a BioAnalyst 2100 system (Agilent, Santa Clara, CA, USA). Finally, the sequencing library was sequenced on a Hiseq platform (Illumina) by Shanghai Personal Biotechnology Cp. Ltd.

4.11. Mitochondrial depolarization

Mito tracker Red was used as a fluorescent probe to detect the drug entering mitochondria. B16 cells incubated in confocal petri dishes were treated with IC_{50} concentration of **Ir1**, **Ir2** and **Ir3** for 4 h, respectively. Then the cells were stained with Mito Tracker Red FM (ThermoFisher, 100 nM) and photographed under laser confocal microscope (Leica, TCS SP8 SR).

Mitochondrial membrane potential (MMP) assay: B16 cells were seeded into 12-well plates (5×10^5 cells) overnight. The cells were treated with IC_{50} concentration of **Ir1**, **Ir2** and **Ir3** for 24 h. The cells were washed three times with cool PBS and stained with 5,5′,6,6′-tetrachloro-1,1′-3,3′-tetrethylbenzimidalylcarbocyanine iodide (JC-1), the cells were then observed under the ImageXpress R Micro XLS System (MD company, USA) and quantitatively analyzed by flow cytometry (Beckman Instruments, NJ). Carbonylcyanide-m-chlorophenyl hydrazone (CCCP) was used as a positive control.

4.12. Reactive oxygen species levels

B16 cells were placed in confocal Petri dishes at a density of 5×10^4 overnight. Then the cells were exposed to IC_{50} concentration of **Ir1**, **Ir2** and **Ir3** for 24 h, thereafter, the cells were washed three times with cool PBS and stained with 2′,7′-dichlorodihydrofluorescein diacetate (DCFH-DA, 1:1000) and observed under the laser confocal microscope (Leica, TCS SP8 SR).

4.13. Apoptosis assay by Annexin V-FITC/PI staining method

When B16 cells in the 6-well plate entered the exponential growth phase, the cells were treated with IC_{50} concentration of **Ir1**, **Ir2** and **Ir3** for 24 h. After trypsinization and centrifugation, the cells were washed twice with PBS. Then, re-suspended in 195 μL of 1 × Annexin V-FITC binding buffer. Next, 10 μL of propidium iodide (PI) and 5 μL of Annexin-FITC were sequentially added to each sample, and the cells were analyzed by flow cytometer (Beckman Instruments, NJ).

4.14. Cell cycle arrest determination

Exponentially growing B16 cells were exposed to IC_{50} concentration of **Ir1**, **Ir2** and **Ir3** for 24 h in the 6-well plates, respectively. The cells were trypsinized and fixed with 75% ethanol overnight at 4 °C. Then, the cells were washed twice with cold PBS, re-suspended in 190 μL of PBS buffer containing 4 μL of PI (1 mg/mL), 4 μL of RnaseA (10 mg/mL) and 0.2 μL of Triton X-100. The cells were analyzed by flow cytometry (Beckman Instruments, NJ).

4.15. Glutathione (GSH) measurement

B16 cells were inoculated in 6-well plates (5×10^5 cells per well) and treated with $2IC_{50}$ concentration of **Ir1**, **Ir2**, **Ir3** for 24 h. Cells were collected by trypsinization and GSH levels were measured by GSH assay kit (Beyotime Biotech, Shanghai, China).

4.16. DNA damage experiment

The cells were seeded into 12-well plates overnight, the cells were treated with IC_{50} concentration of **Ir1**, **Ir2**, **Ir3** for 24 h, Then, the cells were fixed with 75% ethanol and washed three times with PBS, then added blocking buffer for immunol staining (Beyotime Biotechnology, China) to block the cells for 30 min. Primary antibody was added and incubated overnight at 4 °C, then fluorescent secondary antibody and Hoechst were added and incubated for 1 h at 37 °C. Finally, the cells were observed under Xpress Micro XLS. Next, we used Western blot to analyze the expression of γ-H2AX in B16 cells.

4.17. Western blot analysis

B16 cells were seeded into 6-well plates (5×10^5 cells per well) for 24 h and incubated with IC_{50} concentration of the complexes for 24 h. Then the cells were harvested in lysis buffer. After sonication, the samples were centrifuged for 20 min at 13,000 g. The protein concentration of the supernatant was determined by BCA (bicinchoninic acid) assay. Sodium dodecyl sulfate-polyacrylamide gel electrophoresis loaded an equal amount of protein per lane was performed. Gels were then transferred to poly (vinylidene difluoride) membranes (Millipore) and blocked with 5% non-fat milk in TBST (20 mM Tris-HCl, 150 mM

NaCl, 0.05% Tween 20, pH 8.0) (Tris = tris(hydroxymethylaminomethane, Tween = polyoxyethylene monolaurate sorbaitan) buffer for 1 h. The membranes were incubated with primary antibodies at 1:1000 dilutions in 5% non-fat milk at 4 °C overnight, and after washed four times with TBST for a total of 30 min, then the secondary antibodies were conjugated with horseradish peroxidase at 1:1000 dilution for 1 h at room temperature and washed for four times with TBST. The blots were visualized with the Amersham ECL (electrochemiluminescence) and western blotting detection reagents according to the manufacturer's instructions. To assess the presence of a comparable amounts of proteins in each lane, the membranes were stripped finally to detect the β-actin.

4.18. Anti-tumor experiment in vivo

C57BL/6 mice were provided by Guangdong Medical Laboratory Animal Center (Guangzhou, China). B16 cells were cultivated in Dulbecco's modified Eagle medium (DMEM, Gibco) containing 10% fetal calf serum and penicillin (100 U/mL)/streptomycin (0.1 mg/mL) (Gibco) at 37 °C in 5% CO_2. The mice were randomly divided into 3 groups ($n = 5$). To obtain the tumor model, B16 cells were subcutaneously injected into the underarm of each mouse. After 10 days, **Ir1** (2, 3 and 5 mg/kg) was administered intraperitoneal (i.p.) daily. The tumor size and the weight of the mice were recorded every day. At the end of the administration, all mice were executed. The lung, heart, liver, brain, kidney, and spleen of mice were dissected and analyzed. The tumors were excised, and the inhibitory rate was calculated according to the following equation:

$$[(W_1 - W_2)/W_1] \times 100\%$$

W_1 is the average tumor weight in the control group, W_2 is the average tumor weight in the treated group.

4.19. Statistical analysis

Data are expressed as mean ± standard deviation (SD), and each value in this study was obtained from three independent experiments repeated. $^*P < 0.05$ was considered a statistically significant difference.

Declaration of competing interest

The authors declare that they have no known competing financial interests or personal relationships that could have appeared to influence the work reported in this paper.

Data availability

Data will be made available on request.

Acknowledgements

This work was supported by the National Nature Science Foundation of China (No 21877018).

Appendix A. Supplementary data

Supplementary data to this article can be found online at https://doi.org/10.1016/j.ejmech.2022.115046.

Abbreviations

A549	human lung carcinoma
AKT	protein kinase B
B16	mouse melanoma cells
BEL-7402	human hepatocellular
Bax Bcl-2	associated x protein
Bcl-2	B-cell lymphoma-2
BCA	bicinchoninic acid
bzq	benzo[*h*]quinolone
cccp	carbonylcyanide-m-chlorophenylhydrazone
Calcein-AM	calcein-acetoxymethylester
DMEM	Dulbecco's Modified Eagle Medium
DMSO	dimethylsulfoxide
DCHF	2′,7′-dichloro-3,6-fluorandiol
DCHF-DA	2′,7′-dichlorodihydrofluorescein diacetate
DCF	dichlorofluorescein
Eca-109	human esophageal cancer cells
EDTA	ethylene diamine tetraacetic acid
FBS	fetal bovine serum
FITC	fluorescein isothiocyanate
HeLa	human cervical cancer cells
ICP-MS	inductively coupled plasma mass spectrometry
JC-1	5,5′,6,6′-Tetrachloro-1,1′,3,3′-tetraethyl-imidacarbocyanine iodide
LO2	human normal hepatocytes
MTT	3-(4,5-dimethylthiazole)-2,5-diphenyltetraazolium bromide
MMP	mitochondrial membrane potential
PBS	phosphate buffer saline
piq	1-phenylisoquinoline
Hppy	2-phenylpyridine
PARP	poly ADP-ribose polymerase
PI3K	phosphatidylinositol-3-kinase
PI	propidium iodide
PMSF	phenylmethylsulfonyl fluoride
RNase	ribonuclease
RIPA	50 mM Tris (pH 7.4), 150 mM NaCl, 1% NP-40, 0.5% sodium deoxycholate
ROS	reactive oxygen species
RPMI	1640 Roswell Park Memorial Institute 1640
SGC-7901	human gastric adenocarcinoma
TMS	tetramethylsilane
Tris	tris(hydroxymethyl)aminomethane
γ-H2AX	phosphorylated histone H2AX

References

[1] B.J. Aragon-Ching, W.L. Dahut, Anti-angiogenesis approach to genitourinary cancer treatment, Update Cancer Therapeut. 3 (2009) 182–188.
[2] C. De Martel, J. Ferlay, S. Franceschi, Global burden of cancers attributable to infections in 2008: a review and synthetic analysis, Lancet Oncol. 13 (2012) 607–615.
[3] J. Hildebrandt, R. Trautwein, D. Kritsch, N. Häfner, H. Görls, M. Dürst, I. B. Runnebaum, W. Weigand, Synthesis, characterization and biological investigation of platinum(II) complexes with asparagusic acid derivatives as ligands, Dalton Trans. 48 (2019) 936–944.
[4] E.S. Antonarakis, A. Emadi, Cancer chemother, Pharmacology 66 (2010) 1–9.
[5] J.J. Cao, Y. Zheng, X.W. Wu, C.P. Tan, M.H. Chen, N. Wu, L.N. Ji, Z.W. Mao, Anticancer cyclometalated iridium(III) complexes with planar ligands: mitochondrial DNA damage and metabolism disturbance, J. Med. Chem. 62 (2019) 3311–3322.
[6] Z.H. Wang, Z.X. Lv, X.C. Liu, Y.T. Yu, J.Y. Chang, R.X. Dong, C.Y. Li, X.A. Yuan, Z. Liu, Anticancer application of ferrocene appended configuration-regulated half-sandwich iridium(III) pyridine complexes, J. Inorg. Biochem. 237 (2022), 112010.
[7] J. Masternak, A. Gilewska, B. Barszcz, I. Łakomska, K. Kazimierczuk, J. Sitkowski, J. Wietrzyk, A. Kamecka, M. Milczarek, Ruthenium(II) and iridium(III) complexes as tested materials for new anticancer agents, Materials 13 (2020) 3491.
[8] H.W. Zhang, X.F. Liao, X.Y. Wu, C.L. Shi, Y.Y. Zhang, Y.H. Yuan, W.L. Li, J. W. Wang, Y.J. Liu, Iridium(III) complexes entrapped in liposomes trigger mitochondria-mediated apoptosis and GSDME-mediated pyroptosis, J. Inorg. Biochem. 228 (2022), 111706.
[9] Y.H. Yuan, C.L. Shi, X.Y. Wu, W.L. Li, C.X. Huang, L.J. Liang, J. Chen, Y. Wang, Y. J. Liu, Synthesis and anticancer activity in vitro and in vivo evaluation of iridium (III) complex on mouse melanoma B16 cells, J. Inorg. Biochem. 232 (2022), 111820.
[10] L.L. Wang, R.L. Guan, L.N. Xie, X.X. Liao, K. Xiong, T.W. Rees, Y. Chen, L.N. Ji, H. Chao, An ER-targeting iridium(III) complex that induces immunogenic cell death in non-small-cell lung cancer, Angew Chem. Int. Ed. Engl. 60 (2021) 4657–4665.

[11] G. Gupta, S. Cherukommu, G. Srinivas, S.W. Lee, S.H. Mun, BODIPY-based Ru(II) and Ir(III) organometallic complexes of avobenzone, a sunscreen material: potent anticancer agents, J. Inorg. Biochem. 189 (2018) 17–29.
[12] Y.Y. Gu, H.Y. Wen, Y.Y. Zhang, L. Bai, Y. Zhou, H.W. Zhang, L. Tian, J. Hao, Y. J. Liu, Studies of anticancer activity in vivo and in vitro behaviors of liposomes encapsulated iridium(III) complex, J. Biol. Inorg. Chem. 26 (2021) 109–122.
[13] W.J. Wang, Y.Y. Ling, Y.M. Zhong, Z.Y. Li, C.P. Tan, Z.W. Mao, Ferroptosis-enhanced cancer immunity by a ferrocene-appended iridium(III) diphosphine complex, Angew Chem. Int. Ed. Engl. 61 (2022), e202115247.
[14] G. Gupta, P. Kumair, J.Y. Ryu, J. Lee, S.M. Mobin, C.Y. Lee, Mitochondrial localization of highly fluorescent and photostable BODIPY-based ruthenium(II), rhodium(III), and iridium(III) metal complexes, Inorg. Chem. 58 (2018) 8587–8595.
[15] W.G. Chen, X.H. Cai, Q. Sun, X.H. Guo, C.M. Liang, H. Tang, H.M. Huang, H. Luo, L.M. Chen, J.C. Chen, Design and synthesis of aptamer-cyclometalated iridium(III) complex conjugate targeting cancer cells, Eur. J. Med. Chem. 236 (2022), 114335.
[16] Y.Y. Zhang, W.D. Fei, H.W. Zhang, Y. Zhou, L. Tian, J. Hao, Y.H. Yuan, W.L. Li, Y. J. Liu, Increasing anticancer effect in vitro and vivo of liposome-encapsulated iridium(III) complexes on BEL-7402 cells, J. Inorg. Biochem. 225 (2021), 111622.
[17] J.S. Nam, M.G. Kang, J. Kang, S.Y. Park, S.J.C. Lee, H.T. Kim, J.K. Seo, O.H. Kwon, M.H. Lim, H.W. Rhee, T.H. Kwon, J. Am. Chem. Soc. 138 (2016) 10968–10977.
[18] C. Fu, Q. Lv, J. Fan, S.M. Wu, M. Lei, X. Zhang, X.R. Li, W. Zhou, Y. Yu, W.S. Ren, C. Z. Zhao, G.J. Liao, Discovery of polypyridyl iridium(III) complexes as potent agents against resistant Candida albicans, Eur. J. Med. Chem. 233 (2022), 114250.
[19] R.P. Paitandi, R.K. Gupta, R.S. Singh, G. Sharma, B. Koch, D.S. Pandey, Eur. J. Med. Chem. 84 (2014) 17–29.
[20] J.P. Liu, C.Z. Jin, B. Yuan, X.G. Liu, Y. Chen, L.N. Ji, H. Chao, Chem. Commun. 53 (2017) 2052–2055.
[21] Y.Y. Zhang, Y. Zhou, H.W. Zhang, L. Tian, J. Hao, Y.H. Yuan, W.L. Li, Y.J. Liu, DNA-binding and evaluation of anticancer activity in vitro and in vivo of iridium (III) polypyridyl complexes, J. Inorg. Biochem. 224 (2021), 111580.
[22] B.B. Chen, N.L. Pan, J.X. Liao, M.Y. Huang, D.C. Jiang, J.J. Wang, H.J. Qiu, J. X. Chen, L. Li, J. Sun, J. Inorg. Biochem. 219 (2021), 111450.
[23] Y. Liu, B. Liu, C.X. Xu, L. He, Y.C. Wan, L.N. Ji, Z.W. Mao, Mitochondria-targeted phosphorescent cyclometalated iridium(III) complexes: synthesis, characterization, and anticancer properties, J. Biol. Inorg. Chem. 25 (2020) 597–607.
[24] F.L. Xie, Z.T. Huang, L. Bai, J.W. Zhu, H.H. Xu, Q.Q. Long, Q.F. Guo, Y. Wu, S. H. Liu, Antitumor activity studies of iridium(III) polypyridine complexes-loaded liposomes against gastric tumor cell in vitro, J. Inorg. Biochem. 225 (2021), 111603.
[25] G. Ludwig, S. Mijatović, I. RanCelović, M. Bulatović, D. Miljković, D. Maksimović-Ivanić, M. Korb, H. Lang, D. Steinborn, G.N.K. Cerović, Eur. J. Med. Chem. 69 (2013) 216–222.
[26] J.Z. Wu, B.H. Ye, L. Wang, L.N. Ji, J.Y. Zhou, R.H. Li, Bis(2,2′-bipyridine) ruthenium(II)complexes with imidazo[4,5-f][1,10]-phenanthroline or 2-phenylimidazo[4,5-f][1,10]phenanthroline, J. Chem. Soc. Dalton Trans. 8 (1997) 1395–1402.
[27] D.J. Adams, L.R. Morgan, Tumor physiology and charge dynamics of anticancer drugs: implications for camptothecin-based drug development, Curr. Med. Chem. 18 (9) (2011) 1367–1372.
[28] G.H. Lu, X.S. Miao, L. Dou, Crosstalk of physiological pH and chemical pK_a under the umbrella of physiologically based pharmacokinetic modeling of drug absorption, distribution, metabolism, excretion, and toxicity, Expet Opin. Drug Metabol. Toxicol. 17 (2021) 1103–1124.
[29] A. Avdeef, Physicochemical profiling (solubility, permeability and charge state), Curr. Top. Med. Chem. 1 (2001) 277–351.
[30] E.H. Kerns, L. Di, Multivariate pharmaceutical profiling for drug discovery, Curr. Top. Med. Chem. 2 (2002) 87–98.
[31] H. van de Waterbeemd, D.A. Smith, B.C. Jones, Lipophilicity in PK design: methyl, ethyl, futile, J. Comput. Aided Mol. Des. 15 (2001) 273–286.
[32] D.T. Manallack, E. Yuriev, D.K. Chalmers, The influence and manipulation of acid/base properties in drug discovery, Drug Discov, Today Technol 27 (2018) 41–47.
[33] Y. Liu, D.A. Peterson, H. Kimura, D. Schubert, Mechanism of cellular 3-(4,5-dimethylthiazol-2-yl)-2,5-diphenyltetrazolium bromide (MTT) reduction, J. Neurochem. 69 (1997) 581–593.
[34] J.W. Wang, H.M. Liu, X.Y. Wu, C.L. Shi, W.L. Li, Y.H. Yuan, Y.J. Liu, D.G. Xing, Induction of apoptosis in SGC-7901 cells by iridium(III) complexes via endoplasmic reticulum stress-mitochondrial dysfunction pathway, J. Biol. Inorg. Chem. 27 (2022) 455–469.
[35] W.L. Li, C.L. Shi, X.Y. Wu, Y.Y. Zhang, H.M. Liu, X.Z. Wang, C.X. Huang, L.J. Liang, Y.J. Liu, Light activation of iridium (III) complexes driving ROS production and DNA damage enhances anticancer activity in A549 cells, J. Inorg. Biochem. 236 (2022), 111977.
[36] L. Bai, W.D. Fei, Y.Y. Gu, M. He, F. Du, W.Y. Zhang, L.L. Yang, Y.J. Liu, Liposomes encapsulated iridium(III) polypyridyl complexes enhance anticancer activity in vitro and in vivo, J. Inorg. Biochem. 205 (2020), 111014.
[37] Y.Y. Gu, L. Bai, Y.Y. Zhang, H.W. Zhang, D.G. Xing, L. Tian, Y. Zhou, J. Hao, Y. J. Liu, Liposome as drug delivery system enhance anticancer activity of iridium(III) complex, J. Liposome Res. 4 (2021) 432–455.
[38] A. Riedl, M. Schlederer, K. Pudelko, M. Stadler, S. Walter, D. Unterleuthner, C. Unger, N. Kramer, M. Hengstschläger, L. Kenner, D. Pfeiffer, G. Krupitza, H. Dolznig, Comparison of cancer cells in 2D vs 3D culture reveals differences in AKT–mTOR–S6K signaling and drug responses, J. Cell Sci. 130 (2017) 203–218.
[39] M. Zoetemelk, M. Rausch, D.J. Colin, O. Dormond, P. Nowak-Sliwinska, Short-term 3D culture systems of various complexity for treatment optimization of colorectal carcinoma, Sci. Rep. 9 (2019) 7103.
[40] Y. Imamura, T. Mukohara, Y. Shimono, Y. Funakoshi, N. Chayahara, M. Toyoda, N. Kiyota, S. Takao, S. Kono, T. Nakatsura, H. Minami, Comparison of 2D- and 3D-culture models as drug-testing platforms in breast cancer, Oncol. Rep. 33 (2015) 1837–1843.
[41] B. Weigelt, C.M. Ghajar, M.J. Bissel, The need for complex 3D culture models to unravel novel pathways and identify accurate biomarkers in breast cancer, Adv. Drug Deliv. Rev. 69–70 (2014) 42–51.
[42] C. Billecke, S. Finniss, L. Tahash, C. Miller, T. Mikkelsen, N.P. Farrell, O. Bögler, Polynuclear platinum anticancer drugs are more potent than cisplatin and induce cell cycle arrest in glioma, Neuro Oncol. 8 (2006) 215–226.
[43] H. Wu, L. Chen, F. Zhu, X. Han, L. Sun, K. Chen, The cytotoxicity effect of resveratrol: cell cycle arrest and induced apoptosis of breast cancer 4T1 cells, Toxins 11 (2019) 731.
[44] S.M. Yoo, Y.K. Jung, A molecular approach to mitophagy and mitochondrial dynamics, Mol. Cell. 41 (2018) 18–26.
[45] R.C. Scaduto Jr., L.W. Grotyohann, Measurement of mitochondrial membrane potential using fluorescent rhodamine derivatives, Biophys. J. 76 (1999) 469–477.
[46] J. Adler, Quantifying colocalization by correlation: the Pearson correlation coefficient is superior to the mander's overlap coefficient, I. Parmryd, Cytometry 77A (2010) 733–742.
[47] J. Yang, J.X. Zhao, Q. Cao, L. Hao, D. Zhou, Z. Gan, L.N. Ji, Z.W. Mao, Simultaneously inducing and tracking cancer cell metabolism repression by mitochondria-immobilized rhenium(I) complex, ACS Appl. Mater. Interfaces 9 (2017) 13900–13912.
[48] K. Elefantova, B. Lakatos, J. Kubickova, Z. Sulova, A. Breier, Detection of the mitochondrial membrane potential by the cationic dye JC-1 in L1210 cells with massive overexpression of the plasma membrane ABCB1 drug transporter, Int. J. Mol. Sci. 19 (2018) 1985.
[49] C.P. LeBel, H. Ischiropoulos, S.C. Bondy, Evaluation of the probe 2',7'-dichlorofluorescin as an indicator of reactive oxygen species formation and oxidative stress, Chem. Res. Toxicol. 5 (1992) 227–231.
[50] E. Georgieva, D. Ivanova, Z. Zhelev, R. Bakalova, M. Gulubova, I. Aoki, Mitochondrial dysfunction and redox imbalance as a diagnostic marker of "free radical diseases", Anticancer Res. 37 (2017) 5373–5381.
[51] Y. Meng, C.W. Chen, M.M.H. Yung, W. Sun, J. Sun, Z. Li, J. Li, Z. Li, W. Zhou, S. S. Liu, A.N.Y. Cheung, H.Y.S. Ngan, J.C. Braisted, Y. Kai, W. Peng, A. Tzatsos, Y. Li, Z. Dai, W. Zheng, D.W. Chan, W. Zhu, DUOXA1-mediated ROS production promotes cisplatin resistance by activating ATR-Chk1 pathway in ovarian cancer, Cancer Lett. 428 (2018) 104–116.
[52] C. Espinosa-Diez, V. Miguel, D. Mennerich, T. Kietzmann, P. Sánchez-Pérez, S. Cadenas, S. Lamas, Antioxidant responses and cellular adjustments to oxidative stress, Redox Biol. 6 (2015) 183–197.
[53] A.L. Ortega, S. Mena, J.M. Estrela, Glutathione in cancer cell death, Cancers 3 (2011) 1285–1310.
[54] E. Desideri, F. Ciccarone, M.R. Ciriolo, Targeting glutathione metabolism: partner in crime in anticancer therapy, Nutrients 11 (2019) 1926.
[55] Q.Y. Yi, W.Y. Zhang, M. He, F. Du, W.Z. Wang, Y.J. Wang, Y.Y. Gu, L. Bai, Y.J. Liu, Anticancer and antibacterial activity in vitro evaluation of iridium(III) polypyridyl complexes, J. Biol. Inorg. Chem. 24 (2019) 151–169.
[56] P.E. Czabotar, G. Lessene, A. Strasser, J.M. Adams, Control of apoptosis by the BCL-2 protein family: implications for physiology and therapy, Nat. Rev. Mol. Cell Biol. 15 (2014) 49–63.
[57] D.L. Vaux, S. Cory, J.M. Adams, Bcl-2 gene promotes haemopoietic cell survival and cooperates with c-myc to immortalize pre-B cells, Nature 335 (1988) 440–442.
[58] T.J. McDonnell, N. Deane, F.M. Platt, G. Nunez, U. Jaeger, J.P. McKearn, S. J. Korsmeyer, Bcl-2-immunoglobulin transgenic mice demonstrate extended B cell survival and follicular lymphoproliferation, Cell 57 (1989) 79–88.
[59] M. Zhou, X. Liu, Z. Li, Q. Huang, F. Li, C.Y. Li, Caspase-3 regulates the migration, invasion and metastasis of colon cancer cells, Int. J. Cancer 143 (2018) 921–930.
[60] X. Feng, Y. Yu, S. He, J. Cheng, Y. Gong, Z. Zhang, X. Yang, B. Xu, X. Liu, C.Y. Li, L. Tian, Q. Huang, Dying glioma cells establish a proangiogenic microenvironment through a caspase 3 dependent mechanism, Cancer Lett. 385 (2017) 12–20.
[61] M. Mukai, T. Kusama, Y. Hamanaka, T. Koga, H. Endo, M. Tatsuta, M. Inoue, Cross talk between apoptosis and invasion signaling in cancer cells through caspase-3 activation, Cancer Res. 65 (2005) 9121–9125.
[62] K. Lauber, E. Bohn, S.M. Kröber, Y.J. Xiao, S.G. Blumenthal, R.K. Lindemann, P. Marini, C. Wiedig, A. Zobywalski, S. Baksh, Y. Xu, I.B. Autenrieth, K. Schulze-Osthoff, C. Belka, G. Stuhler, S. Wesselborg, Apoptotic cells induce migration of phagocytes via caspase-3-mediated release of a lipid attraction signal, Cell 113 (2003) 717–730.
[63] S.W. Wu, C.H. Su, Y.C. Ho, R. Huang-Liu, C.C. Tseng, Y.W. Chiang, K.L. Yeh, S. S. Lee, W.Y. Chen, C.J. Chen, Y.C. Li, C.Y. Lee, Y.H. Kuan, Genotoxic effects of 1-nitropyrene in macrophages are mediated through a p53-dependent pathway involving cytochrome c release, caspase activation, and PARP-1 cleavage, Ecotoxicol. Environ. Saf. 213 (2021), 112062.
[64] J. Yuan, A. Najafov, B.F. Py, Roles of caspases in necrotic cell death, Cell 167 (2016) 1693–1704.
[65] J.A. Fresno Vara, E. Casado, J. de Castro, P. Cejas, C. Belda-Iniesta, M. González-Barón, PI3K/Akt signalling pathway and cancer, Cancer Treat Rev. 30 (2004) 193–204.

[66] Y. Shiloh, Ataxia-telangiectasia and the Nijmegen breakage syndrome: related disorders but genes apart, Annu. Rev. Genet. 31 (1997) 635–662.
[67] M. Goldstein, M.B. Kastan, The DNA damage response: implications for tumor responses to radiation and chemotherapy, Annu. Rev. Med. 66 (2015) 129–143.
[68] S. Sprouse, K.A. King, P.J. Spellane, R.J. Watts, Photophysical effects of metal-carbon σ bonds in ortho-metalated complexes of iridium(III) and rhodium(III), J. Am. Chem. Soc. 106 (1985) 6647–6653.